Soft Matter

ROYAL SOCIETY OF CHEMISTRY

PAPER

View Article Online
View Journal | View Issue

Cite this: *Soft Matter*, 2021, **17**, 4109

Spatial velocity correlations in inertial systems of active Brownian particles

Lorenzo Caprini * and Umberto Marini Bettolo Marconi

Received 29th December 2020,
Accepted 17th February 2021

DOI: 10.1039/d0sm02273j

rsc.li/soft-matter-journal

Recently, it has been discovered that systems of active Brownian particles (APB) at high density organise their velocities into coherent domains showing large spatial structures in the velocity field. This collective behavior occurs spontaneously, *i.e.* is not caused by any specific interparticle force favoring the alignment of the velocities. This phenomenon was investigated in the absence of thermal noise and in the overdamped regime where inertial forces could be neglected. In this work, we demonstrate through numerical simulations and theoretical analysis that velocity alignment is a robust property of ABP and persists even in the presence of inertial forces and thermal fluctuations. We also show that a single dimensionless parameter, such as the Péclet number customarily employed in the description of self-propelled particles, is not sufficient to fully characterize this phenomenon either in the regimes of large viscosity or small mass. Indeed, the size of the velocity domains, measured through the correlation length of the spatial velocity correlation, remains constant when the swim velocity increases and decreases as the rotational diffusion becomes larger. We find that, contrary to the common belief, the spatial velocity correlation not only depends on inertia but is also non-symmetrically affected by mass and inverse viscosity variations. We conclude that in self-propelled systems, at variance with passive systems, variations in the inertial time (mass over solvent viscosity) and mass act as independent control parameters. Finally, we highlight the non-thermal nature of the spatial velocity correlations that are fairly insensitive both to solvent and active temperatures.

1 Introduction

Many systems of biological or technological interest display fascinating spatial velocity correlations extending over lengths larger than the size of the individual constituents. This phenomenon is an example of the intriguing non-equilibrium behavior typical of active[1–3] and granular matter systems[4,5] and is in stark contrast with the observed behavior characteristic of equilibrium colloidal suspensions where the particle velocities are uncorrelated and follow the Maxwell–Boltzmann distribution.

Colonies of bacteria, such as *Bacillus subtilis* or *Myxococcus xanthus*, display spatial velocity correlations exponentially decaying with a correlation length much larger than the typical bacterium size.[6–8] The velocity field of bacteria forms vortex-domains or clusters where the velocities are mutually aligned and continuously rearrange according to different patterns. This phenomenon occurs at large densities and is often called bacterial turbulence and has been mostly investigated in the framework of hydrodynamic phenomenological theories.[9–12] Particle-based numerical studies have reproduced the formation of velocity domains either in models containing an explicit velocity alignment interaction term[13] or in models where the observed rich variety of polar phases[14] was mainly due to the elongated shape typical of many species of bacteria.

Recent experiments with cell monolayers revealed similar spatial structures in the velocity field extending over a range of ~10–20 microns for mesenchymal cells up to ~500 microns. Their size, in the case of very adhesive epithelial cells, reaches ~50 times the one of the single cells.[15] Many cells, such as the typical Madin–Darby Canine Kidney (MDCK) cells[16] or human bronchial epithelial cells (HBEC),[17] are not elongated but still form large groups with correlated velocities often organizing in vortex structures[17,18] (without showing the formation of polar bands) and give rise to velocity correlations exponentially decaying in space.[19,20] To explain these behaviors, several models have been proposed.[21] At the particle level, alignment interactions between particle polarizations or particle velocities have been often included in cell dynamics.[22,23] However, in recent studies, these phenomenological interactions have been replaced by additional frictional forces[19] or complex anti-alignment interactions of biological origin[24] that could also give rise to a similar phenomenology.

Despite their different origins, one common feature of these systems is the formation of domains with correlated velocities even in the absence of the polar bands that instead are typically

School of Sciences and Technology, University of Camerino, Via Madonna delle Carceri, I-62032, Camerino, Italy. E-mail: lorenzo.caprini@gssi.it

observed in Vicsek-like models. At variance with the mentioned theoretical approaches, the local velocity alignment has been recently reproduced *via* the dissipative stochastic dynamics without introducing any explicit alignment interactions between the particle orientations[25–27] or some kind of local interaction between particle velocity and self-propulsion. Dense systems of purely repulsive active Brownian particles (ABP) form domains where the velocities are aligned or arranged in vortex-like patterns when they attain hexatic or solid order[26] or in the dense phase of the non-equilibrium phase-coexistence,[25] known as motility induced phase separation (MIPS).[28–30] ABP already contains the following minimal ingredients producing velocity patterns: (i) persistent self-propulsion forces and (ii) purely repulsive interactions. However, so far, these results have been obtained through theoretical analysis and simulations neglecting two important aspects: the inertial forces and thermal noise due to the molecules of the solvent. In apparent contradiction with the results of ref. 25–27, a successive investigation, based on thermal overdamped ABP[31] and focused on micro-phase motility induced phase separation, did not reveal the presence of spatial velocity correlations. Two natural questions arise: (i) does the velocity alignment in ABP systems occur only in the absence of thermal fluctuations? (ii) Is this ordering suppressed if one takes into account the effect of the acceleration?

We anticipate the main result of the present study: the spatial patterns in the velocity field of active systems survive in the case of underdamped active dynamics and thermal noise. Our investigation also proves three important results derived by combining numerical and theoretical methods:

(i) The inadequacy of the s–o-called Péclet number, as a single active force dimensionless parameter, in understanding the dynamical collective phenomena. Indeed, we unveil the non-symmetric role of persistence time and swim velocity, with the spatial velocity correlation function being independent of the latter but deeply affected by the former.

(ii) Asymmetric role of mass and inverse viscosity in the velocity correlation functions whose changes are not controlled only by the inertial time (mass over viscosity), but depend on both parameters.

(iii) Marginal role of thermal and active temperatures for the dynamical collective phenomena presented so far. The temperature increase does not affect the correlation length of the spatial velocity correlation, revealing a dynamical scenario fairly different from what one expects for equilibrium ferromagnetic systems.

The article is structured as follows: in Section 2, we introduce the model describing the self-propelled system in the underdamped regime and, in Section 3, we present the velocity alignment phenomenology. Sections 4–6 discuss the role of the active force, inertial forces and temperature. Finally, we conclude by summarizing the main results and presenting some final remarks.

2 Model

In order to investigate the collective dynamics of a system of inertial self-propelled particles, we perform numerical simulations of the underdamped version of the ABP model, and build a theoretical framework by employing the Active Ornstein–Uhlenbeck (AOUP) model containing the same deterministic force terms. In the two models, the active forces are different but share similar statistical properties, such as the temporal autocorrelation. We resort to this procedure because it greatly simplifies the theoretical analysis leading also to analytical predictions for the probability distribution function.[32] Both the AOUP and the ABP have been successfully employed to reproduce many aspects of the active matter phenomenology including accumulation near an obstacle,[33–35] spatial velocity correlations,[26,27] entropy production[36–39] and phase-coexistence without attraction.[36,40] The underdamped ABP equation of motion, describing a system of interacting self-propelled particles of mass m, are:

$$\dot{\mathbf{x}}_i = \mathbf{v}_i, \tag{1a}$$

$$m\dot{\mathbf{v}}_i = -\gamma \mathbf{v}_i + \mathbf{F}_i + \mathbf{f}_i^{\mathrm{a}} + \sqrt{2\gamma T}h_i, \tag{1b}$$

where $\mathbf{x}_i$ and $\mathbf{v}_i$ represent the particle position and velocity, respectively. The drag coefficient, γ, and the solvent temperature, T, determine the thermal diffusion coefficient, D_t, *via* the Einstein relation, $\gamma D_t = T/m$. The term η is a white noise vector with zero average and unit variance, accounting for the random collisions between the self-propelled particles and the particles of the solvent, such that $\langle \eta_i(t)\eta_j(t')\rangle = \delta(t - t')\delta_{ij}$. As for equilibrium colloids, the solvent exerts a Stokes drag force proportional to $\mathbf{v}_i$. Often, the thermal diffusivity of active colloidal and bacterial suspensions[41] is negligible compared to the effective diffusivity produced by the active force. The effect of inertia is also considered not to be important in the case of typical active particles such as microscopic self-propelled colloids or bacteria swimming in solution. However, this approach needs to be reconsidered in the light of recent studies focused on the interplay between inertia and active forces[42–48] motivated by the existence of experimental macroscopic systems, such as vibro-robots[49,50] or camphor surfers[51] which behave as active particles.

The particle interactions are represented by force, $\mathbf{F}_i = -\nabla_i U_{\mathrm{tot}}$, where $U_{\mathrm{tot}} = \sum_{i<j} U\left(\left|\mathbf{x}_i - \mathbf{x}_j\right|\right)$ is a pairwise potential. We choose U as a shifted and truncated Lennard-Jones potential:[26,52]

$$U(r) = 4\varepsilon\left(\left(\frac{\sigma}{r}\right)^{12} - \left(\frac{\sigma}{r}\right)^{6}\right), \tag{2}$$

for $r \leq 2^{1/6}\sigma$ and zero otherwise.

The constants ε and σ determine the energy unit and the nominal particle diameter, respectively. In the spirit of minimal modeling, the self-propulsion is represented through a stochastic force, namely $\mathbf{f}_i^{\mathrm{a}}$. At this level of description, the details about the chemical or mechanical origin of the self-propulsion[1,3,41,53] are not specified. This force drives the system far from equilibrium[36,54] and determines a persistent motion in a random direction lasting for a time smaller than a characteristic persistence time, τ. The two dimensional ABP self-propulsion

is a force with constant modulus f_0 and time-dependent orientation $\mathbf{n}_i = (\cos\theta_i, \sin\theta_i)$:

$$\mathbf{f}_i^{\mathrm{a}} = f_0 \mathbf{n}_i. \tag{3}$$

The angle θ_i performs a Brownian motion:

$$\dot{\theta}_i = \sqrt{2D_{\mathrm{r}}}\chi_i, \tag{4}$$

where χ_i is a white noise with zero average and unit variance and $D_{\mathrm{r}} = 1/\tau$ a rotational diffusion coefficient determining how persistent is the propagation direction. The parameter f_0 fixes the swim velocity induced by self-propulsion:

$$v_0 = \frac{f_0}{\gamma}. \tag{5}$$

Finally, we introduce the active temperature:

$$T_{\mathrm{a}} = f_0{}^2\frac{\tau}{\gamma} = \gamma\tau v_0{}^2. \tag{6}$$

in agreement with previous definitions employed for overdamped active dynamics.[44,55] This parameter will play a relevant role in the following.

The AOUP model[56–64] employed to ease the theoretical analysis replaces the ABP self-propulsion (3) by an Ornstein–Uhlenbeck process:

$$\tau\dot{\mathbf{f}}_i^{\mathrm{a}} = -\mathbf{f}_i^{\mathrm{a}} + f_0\sqrt{2\tau}\xi_i, \tag{7}$$

where ξ_i is a white noise vector with zero average and unit variance, such that $\langle \xi_i(t)\xi_j(s)\rangle = \delta_{ij}\delta(t-s)$. In the AOUP, the modulus of $\mathbf{f}_i^{\mathrm{a}}$ is not held rigidly fixed but fluctuates around the mean value f_0. The correlation time, τ, of the active force, is chosen to have a common value in AOUP and ABP.[65,66] In both models the self-correlation of the active force decays in time with an exponential law.

Regarding the aptness of the AOUP for adequately reproducing the salient features of the ABP, we mention a recent study[67] of the single-particle velocity distribution in the case of dense active solid configurations, similar to those analyzed in this paper. In that work, we concluded that in the large persistence regime (*i.e.* for a broad range of τ including the values analyzed in this work) the ABP single-velocity properties are well-described by those of an AOUP system at variance with the small persistence regime.

3 Velocity alignment

We have integrated numerically eqn (1) and eqn (4) for a system of N particles moving in a square domain of size L under periodic boundary conditions. The simulations are performed keeping fixed the packing fraction $\phi = N/L^2\sigma^2\pi/4$ in such a way that the system attains a solid configuration without showing changes in the positional structure of the system for a broad range of activity parameters (both f_0 and D_{r}). Indeed, it is known that the increase of both f_0 (or equivalently of v_0) and τ induces the solid–hexatic and finally the hexatic–liquid transition.[26,68,69] A further increase of f_0 and τ leads to a non-equilibrium phase-coexistence that, at variance with passive Brownian particles, occurs even in the absence of attractive interactions.[70–76] This phenomenon, known as motility induced phase separation (MIPS), is due to the particle slowdown caused by interactions.[52]

Ref. 25 and 26 (for a phase-separated and homogeneous liquid, hexatic and solid configurations, respectively) demonstrated the spontaneous occurrence of velocity alignment in the case of athermal ABP in the overdamped regime despite the absence of any form of alignment interaction. As a first result, we show that the spontaneous velocity alignment occurs even in the case of the underdamped dynamics modeled by eqn (1), that accounts for both the finite particle acceleration and thermal fluctuations induced by the solvent. Fig. 1 shows a pair of snapshots illustrating the comparison between a system governed by eqn (1) with $\gamma = 10^2$ and $m = 1$ and a system evolving with the overdamped dynamics whose details are reported in Appendix A. In particular, in panels (b) and (c), the color-map represents the velocity direction of each particle, while panels (d) and (e) show the orientation of the self-propulsion. In the former case, the particles are colored according to the angle formed by the velocity $\mathbf{v}_i$ of each particle with the x axis, while, in the latter case, according to the angle θ_i of the self-propulsion. While the self-propulsion directions are random without showing any spatial structure (as expected from eqn (4)), large domains containing aligned velocities are observed. This means that $\mathbf{v}_i$ does not coincide with $\mathbf{f}_i^{\mathrm{a}}$ in dense configurations where the interparticle interactions are not rare events. The same scenario could be detected in the bulk of the dense phase of MIPS that reaches very large packing fractions attaining configurations that could even display the hexatic or almost-solid orders.[25]

To quantify the size of the velocity domains, we study the spatial velocity correlation function, $C(r)$, defined as:

$$C(r) = \frac{\langle \mathbf{v}(r)\cdot\mathbf{v}(0)\rangle}{\langle \mathbf{v}^2\rangle},$$

normalized by dividing with the velocity variance, $\langle \mathbf{v}^2\rangle$. The associated correlation length provides a measure of the average size of a velocity domain since particles not belonging to the same domain display uncorrelated velocities. The observable $C(r)$ is reported in Fig. 1(a) for two different values of D_{r} both for the underdamped and the overdamped dynamics for large values of γ such that the inertial forces play a marginal role. Two values of D_{r} are reported, such that $\tau = 1/D_{\mathrm{r}} \gg m/\gamma$, and both reveal a fair agreement between overdamped and underdamped dynamics. As already shown in ref. 26, the spatial velocity correlation decreases more slowly as D_{r} is increased, in particular, the correlation length scales as $\tau^{1/2}$ with $\tau = 1/D_{\mathrm{r}}$ in the overdamped regime. How this scaling with τ would be modified due to inertial effects is described in Section 5.

3.1 Theoretical prediction

We have extended to the dynamics (1) the analytical method previously employed in the study of the spatial velocity correlation functions in the case of overdamped ABP in dense configurations.[25–27] The details of the calculations are reported in Appendix B and lead to the following formula for the Fourier transform of the steady-state equal-time velocity correlation obtained by assuming the solid phase through the 6-fold

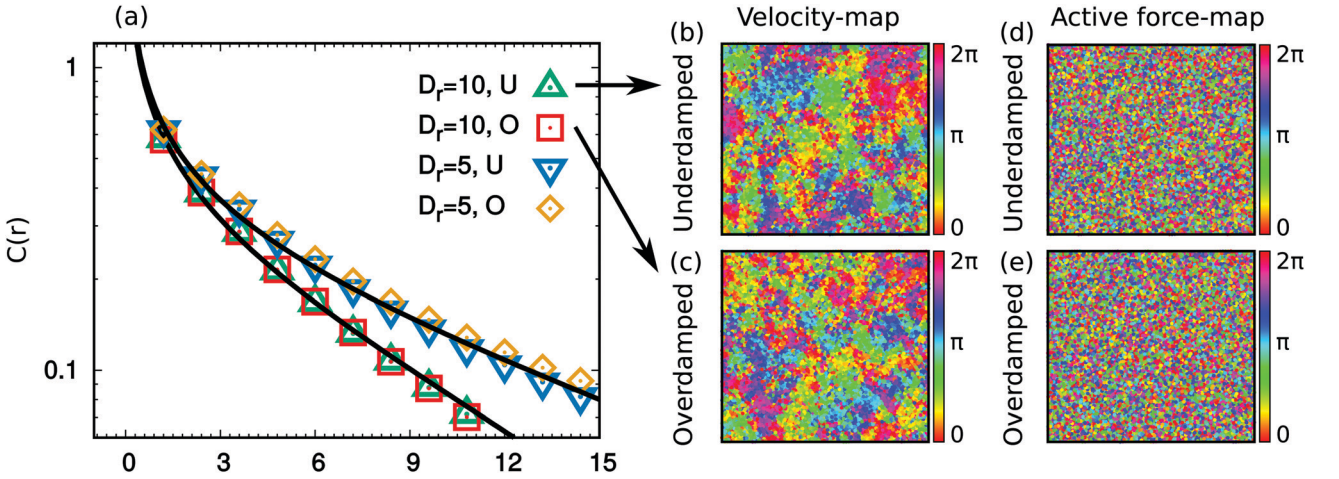

Fig. 1 Comparison between the velocity domains of overdamped and underdamped dynamics. Panel (a): Spatial velocity correlation, $C(r) = \langle \mathbf{v}(r)\cdot\mathbf{v}(0)\rangle/\langle \mathbf{v}^2\rangle$, for two different values of D_r, as detailed in the legend. For both values, we compare the correlation obtained *via* underdamped dynamics eqn (1) (denoted by the symbol U) with the one corresponding to overdamped dynamics eqn (15) (symbol O). The dashed black lines represent the theoretical predictions, obtained by fitting the functional form given by eqn (10) with the function $f(r) = ae^{-r/\lambda}/r^{1/2}$, where λ is given by eqn (11) and a and b are two positive fitting parameters. Panel (b–e): Snapshot configurations for $D_r = 10$ relative to underdamped dynamics (panels (b and d)) and to overdamped dynamics (panels (c and e)). Particles are colored according to the velocity direction in panels (b) and (c) and according to the orientational angle, θ (identifying the direction of the active force), in panels (d) and (e), respectively. The velocity vector in the overdamped case is represented by $\dot{\mathbf{x}}$ as described in Appendix A. The simulations have been obtained using $\phi = 1.1$ with $N = 10^4$. The other parameters are $\gamma/m = 10^2$, $\varepsilon = 10^2$, $\sigma = 1$, $T = 10^{-1}$, and $f_0 = 5 \times 10^3$, corresponding to a swim velocity of $v_0 = 50$. We also mentioned that the simulation with $D_r = 10, 5$ corresponds to Peclet numbers, $\mathrm{Pe} = v_0/(D_r\sigma) = 10, 20$, respectively.

symmetry:

$$\langle \hat{\mathbf{v}}(\mathbf{q})\cdot\hat{\mathbf{v}}(-\mathbf{q})\rangle = \frac{2T}{m} + \frac{2T_a}{m}\frac{1}{1+\tau/\tau_I}\frac{1}{1+\dfrac{\tau^2}{1+\tau/\tau_I}\omega^2(\mathbf{q})} \tag{8}$$

where $\tau_I = m/\gamma$ is the inertial time and T_a the active temperature, defined in eqn (6). The vector $\mathbf{q}$ is a vector of the Fourier space and $\hat{\mathbf{v}}(\mathbf{q})$ is the Fourier transform of the velocity vector. The frequency $\omega(\mathbf{q})$ in the long-wavelength limit, $\mathbf{q} \to 0$, reduces to:

$$\omega^2(\mathbf{q}) \approx \frac{3\omega_E{}^2}{2}\bar{x}^2\mathbf{q}^2 \tag{9}$$

with

$$\omega_E{}^2 = \frac{1}{2m}\left(U''(\bar{x}) + \frac{U'(\bar{x})}{\bar{x}}\right).$$

The terms $U'(\bar{x})$ and $U''(\bar{x})$ represent the first and the second derivatives of U calculated at $\bar{x}$, the average distance between two nearest neighbor particles. The full expression for $\omega^2(\mathbf{q})$ is reported in Appendix B.

Using formula (9), we can find (see Appendix C) the following expression for the real space velocity correlation, holding for large distances (at least, $r > \sigma$):

$$C(r) \approx \frac{2}{\langle \mathbf{v}^2\rangle}\frac{T_a}{m}\frac{1}{1+\tau/\tau_I}\frac{\bar{x}^2}{\lambda^2}\left(\frac{\lambda}{8\pi r}\right)^{1/2} e^{-r/\lambda}, \tag{10}$$

where the correlation length λ is given by

$$\lambda^2 = \frac{3}{2}\bar{x}^2\frac{\omega_E{}^2\tau^2}{1+\dfrac{\tau}{\tau_I}}. \tag{11}$$

The overdamped result derived in ref. 25–27 is recovered in the limit $\tau_I \ll \tau$, *i.e.* when the solvent viscosity is sufficiently large (or the particle mass sufficiently small) compared to the persistence time of the active force.

For some choices of the parameters of the active force, it is possible to obtain large values of λ so that a huge group of particles moves in the same direction. Hence, to exclude the undesired finite-size effects, we always performed simulations in such a way that the condition $L \gg \lambda$ is satisfied (in particular, the ratio L/λ is not smaller than 10 for the whole range of parameters analyzed). This condition guarantees that the spatial velocity correlation approaches zero by avoiding finite-size effects and is fundamental to get results consistent with the theoretical analysis. If this condition is not fulfilled, particles could form a single velocity domain (spanning the entire simulation box) oriented in a direction that changes with a typical time $\propto \tau$. This state is known as active traveling crystals[77–79] and disappears performing simulations with larger boxes.

On the other hand, eqn (10) displays a non-physical divergence at the origin and does not correctly reproduce the behavior of $C(r)$ for small separations, namely $r < \sigma$. The divergence is determined by the absence of an upper cutoff in the $\mathbf{q}$-integral that is used to derive analytically the Fourier anti-transform of eqn (8). The divergence disappears by considering the correct integration limits when anti-transforming eqn (8). In Appendix D, we calculate the variance of the velocity distribution employing the exact expression of $\omega(\mathbf{q})$ and obtain the analytical expression of the kinetic temperature, $T_k = m\langle \mathbf{v}^2\rangle/2$, in the presence of inertial forces and thermal noise:

$$T_k = T + \frac{T_a}{1+\tau/\tau_I+6\omega_E{}^2\tau^2}\frac{\mathscr{J}}{\pi}, \tag{12}$$

where the term $\mathscr{J}$ is a function of τ, τ_I and ω_E. The term in eqn (12) is reported in Appendix D and contains the complete elliptic integral of the first kind. Here, we just stress that does not show any dependence on T_a or T. Formula (12) generalizes the overdamped result of ref. 67, (derived for overdamped ABP, such that $\tau_I \ll \tau$), and provides an analytical prediction for the kinetic temperature.

We remark that the predictions regarding the spatial velocity correlations and kinetic temperature hold in the solid-like regime and, as already shown in ref. 26, break down when the solid–hexatic transition takes place and the number of defects becomes statistically relevant. In addition, expression (10) can be used to extract λ from simulations through numerical fits for comparison with prediction (11).

In the next sections, we report an extensive numerical study by varying both the parameters of the active force and inertial force, taking advantage of the comparison with our theory. The effect of the density increase has been already discussed in ref. 26 where the phase diagram (packing fraction, ϕ, *vs.* τ plotting λ as a color gradient) has been reported. In this paper, we do not perform numerical investigation by varying density but recall that the larger the ρ, the larger the λ. In the solid-like phase, this is consistent with eqn (11), since the increase of ρ leads to decrease of $\bar{x}$ and, thus, the increase of the factor $U''(\bar{x}) + U'(\bar{x})/\bar{x}$ appearing in the expression for $\omega_E{}^2$ that is proportional to λ.

4 Role of the self-propulsion

In ABP systems, the degree of activity is often accounted for by a single dimensionless parameter, the so-called Péclet number, $\mathrm{Pe} = v_0/(D_r\sigma)$, so that the decrease of D_r has the same effect as the increase of v_0. Actually, most of the studies concerning systems of interacting ABP are obtained *via* this procedure and the ABP phase diagram is usually described in terms of two parameters: density and Péclet number.[43,69,80–82]

Herein, we demonstrate that variations of v_0 and $1/D_r$ are not interchangeable, as far as the spontaneous velocity alignment is concerned. We show that a single parameter, the Péclet number, is unable to fully capture the non-equilibrium dynamical properties of active particles. In a previous study on the dense phases of overdamped ABP,[26] the role of τ at fixed self-propulsion was investigated numerically and the results were found to be in agreement with the theoretical predictions ($\lambda \propto \tau^{1/2} \propto 1/D_r^{1/2}$). This could suggest that λ increases as Pe grows. We study the velocity correlation function by varying the self-propulsion intensity, f_0 (and, thus, v_0), and keeping fixed the remaining parameters and, D_r, in particular, so that Pe increases as shown in Fig. 2(a). In Fig. 2(b), we display the correlation length, λ, measured by fitting the functional form reported in eqn (11). This procedure reveals that $C(r)$ and λ are not affected by the increase of f_0 for a broad range of f_0 values for which the system remains in solid-like configurations. In other words, the correlation length (and, thus, the size of the velocity domains) remains constant when Pe is increased by changing v_0 but the increased Pe is changed through $D_r = 1/\tau$.

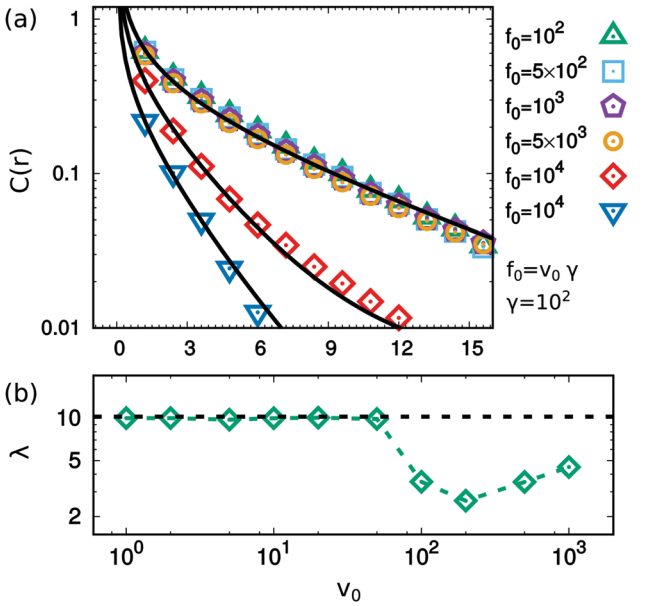

Fig. 2 Spatial velocity correlation as a function of self-propulsion intensity. Panel (a): Spatial velocity correlation, $C(r)$, for different values of the self-propulsion intensity, $f_0 = v_0\gamma$. The dashed black lines are the theoretical predictions, obtained by fitting the functional form given by eqn (10) *via* the function $f(x) = ae^{-r/\lambda}/r^{1/2}$, where λ is given by eqn (11) and a is a positive fitting parameter. Panel (b): Correlation length, λ, of $C(r)$ as a function of v_0. The value of λ has been obtained by fitting the function $f(r) = ae^{-r/c}/r^{1/2}$, fitting also the constant c to be compared with λ. The dashed black line has been obtained evaluating eqn (11) with the set of parameters of the simulation, where $\bar{x}$ has been measured numerically and reads $\bar{x} = 0.91$. The parameters employed in the numerical study are $\phi = 1.1$ with $N = 10^4$, $\gamma = 10^2$, $m = 1$, $\varepsilon = 10^2$, $\sigma = 1$, $T = 10^{-1}$ and $D_r = 10$. Since the Péclet number is defined as $\mathrm{Pe} = v_0/(D_r\sigma)$, we remark that it varies from $\mathrm{Pe} = 10^{-2}$ to $\mathrm{Pe} = 10^2$, in panel (b), and that the hexatic phase is observed for $\mathrm{Pe} \geq 5$ (corresponding to $f_0 \geq 5 \times 10^3$ and $v_0 \geq 50$).

As a result, Pe cannot be a good dimensionless parameter suitable to describe the spatial velocity correlation. When f_0 exceeds a threshold value (that in Fig. 2 is $f_0 > 5 \times 10^3$ corresponding to $v_0 = 50$), the function $C(r)$ decays faster just because a solid–hexatic transition takes place but still maintains the functional form (10). The faster decay, corresponding to a decrease in the correlation length, is not surprising since the lack of orientational order in the hexatic phase and periodic order in the liquid phase has been recognized as one of the main reasons for λ decrease.[26] Further details on the occurrence of the solid–hexatic transition in this system are reported in Appendix E. In the literature (see for instance ref. 26, 68 and 69), the positional order of the system has been studied in terms of the Péclet number ($\propto v_0/D_r$), implicitly assuming that the increase of v_0 can be mapped onto the decrease of D_r. However, to the best of our knowledge, there is no quantitative validation of the symmetric action of v_0 and $1/D_r$ on the full phase diagram of ABP. In other words, it is not clear if, by varying Pe through v_0 (at fixed D_r) or $1/D_r$ (at fixed v_0), the solid–hexatic and hexatic–liquid transition lines of the phase diagram could be modified. Instead, this problem has been recently addressed regarding the MIPS transition line which results affected by the protocol used to vary

the Péclet number.[83] It is likely that the homogeneous phases could also be affected by the procedure employed to change.

Finally, for values of f_0 producing spatial inhomogeneity (namely for $f_0 > 2 \times 10^4$ corresponding to $v_0 > 2 \times 10^2$), λ increases again revealing a non-monotonic behavior. This effect is due to the phase-separation inducing a local increase in the density and thus the growth of λ in the denser phase, as already observed in ref. 26.

We also stress that our numerical results in the solid phase are supported by the main prediction, eqn (10) and (11). Indeed, the correlation length, λ, does not contain an explicit dependence on f_0 (and, thus, v_0). This parameter appears as a simple prefactor in the shape of $\langle \mathbf{v}(r)\cdot\mathbf{v}(0)\rangle$, specifically, through the active temperature. Thus, it cannot deeply affect the occurrence of velocity alignment, except for values of f_0 comparable with T as shown in detail in Section 6.

5 The asymmetric role of mass and viscosity

In passive systems, the role of inertial forces could be encapsulated in a single parameter, the inertial time, $t_I = m/\gamma$, corresponding to the ratio between the mass and solvent viscosity. This time controls the relaxation towards equilibrium but does not affect the steady-state properties of the system. By contrast, as we show hereafter, in the ABP case, the scenario is different revealing the non-symmetric role played by mass and inverse viscosity, and their influence on the steady-state properties of the system and the dynamical collective phenomena reported so far.

Fig. 3(a) displays the correlation length, λ, numerically extracted from $C(r)$ for different values of τ_I. The green and orange curves are obtained by varying m at fixed γ and by varying γ at fixed m, respectively, and clearly show different results for the same τ_I but different values of m and γ. In particular, if τ_I is increased by varying γ, λ reaches a constant value, while if τ_I is increased by varying m, λ monotonically decreases with m. This is consistent with the prediction (11), that in the underdamped regime where the inertial time is the larger one, $\tau_I \gg \tau$, and explicitly reads:

$$\lambda_u^2 = \bar{x}^2 \frac{3\tau^2}{4m}\left(U''(\bar{x}) + \frac{U'(\bar{x})}{\bar{x}}\right). \quad (13)$$

On the contrary, if τ_I is decreased by varying γ, λ monotonically decreases while, if τ_I is decreased by varying m, λ approaches a constant value, consistently with the outcome of eqn (11), in the overdamped regime, *i.e.* when $\tau_I \ll \tau$:

$$\lambda_o^2 = \bar{x}^2 \frac{3\tau}{4\gamma}\left(U''(\bar{x}) + \frac{U'(\bar{x})}{\bar{x}}\right). \quad (14)$$

This asymmetric role of mass and inverse viscosity is a pure non-equilibrium effect without a passive counterpart suggesting that a single parameter is not enough to describe the dynamical properties of far equilibrium systems.

In Fig. 3(b), we display λ as a function of τ for two different values of γ and $m = 1$ to evaluate how inertial forces affect the scaling with the persistence time of the active force. At first, we observe that the effect of the inertial forces is to reduce the correlation length of the spatial velocity correlation through the constant prefactor $1/(1 + \tau_I/\tau)$ appearing in the expression of λ^2, eqn (11). The comparison between the overdamped prediction, eqn (14) (dashed lines), and the numerical data (points) reveals a fair agreement with the prediction of eqn (11) (solid lines).

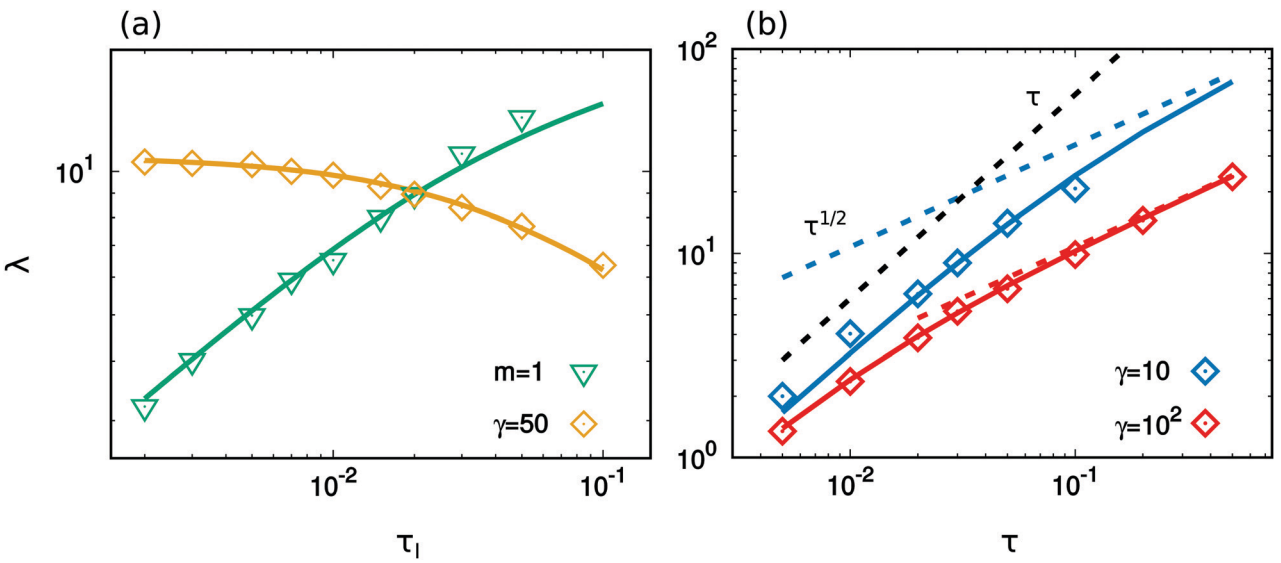

Fig. 3 Correlation length for different values of mass and viscosity. Panel (a): Correlation length, λ, of $C(r)$ as a function of the inertial time, τ_I at fixed τ = 0.1. The green and yellow data have been obtained by varying γ at m = 1 and m at γ = 50. Panel (b): λ as a function of the persistence time, τ, for two different values of γ = 10 (blue points) and 10^2 (red points) with m = 1. In both panels, the points are obtained from numerical simulations while the solid lines from theoretical prediction, eqn (11). The dashed blue and red lines in panel (b) are obtained from eqn (14) and, finally, the dashed black line is an eye-guide to evidence the linear behavior with τ. The numerical values of λ have been obtained by fitting the function $f(r) = ae^{-r/c}/r^{1/2}$, where c is the estimate of λ. The remaining parameters of the simulations are ϕ = 1.1, $N = 10^4$, $\varepsilon = 10^2$, σ = 1, $T = 10^{-1}$ and $f = 5 \times 10^3$.

The prefactor approaches 1 in the overdamped regime, for $\tau_I \ll \tau$, giving rise to the behavior $\lambda \propto \tau^{1/2}$ that has been already reported in ref. 26. For $\tau \leq \tau_I$, the inertia starts playing a role in decreasing the value of λ. For very small values of τ_I, inertial effects cannot be appreciated since they could be observed only when τ is such that $\lambda < \sigma$ corresponding to particle velocities at different positions almost uncorrelated. In this regime of parameters, $\lambda \propto \sqrt{\tau}$ in the whole range of τ where the velocity field has a spatial structure. On the contrary, eqn (13) shows that in the regime $\tau_I \gg \tau$, the prefactor reduces to τ^2/m in such a way that $\lambda \propto \tau$. Thus, when τ_I is large, the correlation length displays two distinct regimes with τ that are shown in Fig. 3(b), for $\gamma = 10$ (red curve): a linear increase for small values of τ, such that when $\tau_I \gg \tau$, is followed by the overdamped scaling, $\lambda \propto \tau^{1/2}$, always occurring in the opposite regime, $\tau_I \ll \tau$.

6 Role of the temperature

The temperature, T, is crucial in determining whether it is possible to detect the spontaneous velocity alignment and the occurrence of spatial velocity correlations. Fig. 4 shows $C(r)$ at fixed f_0 and D_r, for different values of T and keeping fixed γ and m (and, thus, T_a). Interestingly, $C(r)$ decays with distance at the same rate, but its amplitude decreases until it approaches an almost flat vanishing shape when T is sufficiently large. Our observations are in agreement with the theoretical prediction (10), as shown by the comparison between points and solid lines in Fig. 4. In particular, in panel (a) the insensitivity of λ to changes of T is numerically corroborated by comparing with the theoretical prediction. The solvent temperature T only affects the amplitude of the normalized spatial profile of the velocity correlation entering the analytical expression for $C(r)$ just through the term $\langle \mathbf{v}^2 \rangle$ (proportional to T_k, eqn (12)). Indeed, its value increases when T grows at variance with the expression $\langle \mathbf{v}(r) \cdot \mathbf{v}(0) \rangle$, which remains unchanged for $r > \sigma$ (eqn (10)).

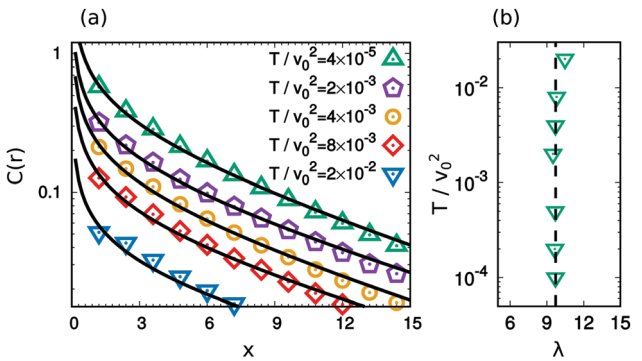

Fig. 4 Panel (a): Spatial velocity correlation, $C(r)$, for different values of the self-propulsion intensity, $f_0 = v_0\gamma$. The dashed black lines are the theoretical predictions, obtained by fitting the functional form given by eqn (10) *via* the function $f(r) = ae^{-r/\lambda}/r^{1/2}$, where λ is given by eqn (11) and a is a fitting parameter. Panel (b): T/v_0^2 *vs.* correlation length, λ. The values of λ have been extracted from the data fitting the function $f(r) = ae^{-r/c}/r^{1/2}$, fitting also the constant c. The simulations are obtained with the following parameters: $\phi = 1.1$, $N = 10^4$, $\sigma = 1$, $\gamma = 10^2$, $m = 1$, $\varepsilon = 10^2$, $v_0 = 50$, and $D_r = 10$.

Hence, the amplitude of $C(r)$ for each $r > \sigma$ is controlled by the ratio T_a/T, through a function $\propto 1/(T/T_a + \alpha)$ where α is constant with respect to T and T_a. To summarize, a change in the solvent temperature can be mapped onto a change of the active temperature so that the relative contribution of the active and thermal fluctuations is mainly controlled by the non-dimensional ratio T_a/T.

While these conclusions apply to solid-like configurations, we argue that the transition from solid-like to hexatic-like behavior does not occur in the same broad range of temperatures observed in the passive systems ($f_0 = 0$), due to the larger values of the packing fraction considered in this study.

Finally, some authors claimed the need to use alignment interactions to get consistent spatial structures in the velocity correlations[23] or asserted that their numerical simulations did not produce any evidence of the existence of velocity domains.[31] We believe that these claims are a consequence of the range of temperatures considered in their numerical system, which were perhaps too large compared to T_a according to the predictions (10) and (12). Another relevant cause motivating these claims could be the lack of periodic order, as it occurs in homogenous active liquids.

7 Conclusion

In this article, we have studied the solid and the dense cluster regimes of a system of interacting active particles evolving according to the underdamped version of the active Brownian particles model. Our first target was shedding light on an emergent collective phenomenon, namely, the spatial ordering of the velocity field. This phenomenon was already observed in systems of overdamped, athermal ABP, but demanded further investigation by using more realistic dynamics. The underdamped dynamics is the natural approach to include the inertial forces and the effect of thermal noise. We confirmed the spontaneous occurrence of velocity domains and quantified their average size by measuring the correlation length of the spatial velocity correlation function. We corroborated our numerical findings employing theoretical arguments analytically predicting both the spatial shape of the velocity correlation and the parameter dependence of its correlation length.

We have also shown that a single dimensionless parameter, such as the Péclet number (usually defined as proportional to the swim velocity and the persistence time) fails to fully describe the velocity alignment phenomenon in dense ABP systems or their phase-separated configurations. A change in the persistence time cannot be mapped onto a change in the swim velocity, in contrast with the widespread opinion in the literature. Indeed, the size of the domains (corresponding to the correlation length of the spatial velocity correlation) increases with the persistence time while it remains constant with the self-propulsion intensity (that is proportional to the swim velocity). Despite the Péclet number having been intensively used to describe the structural properties of the system (usually, the phase diagram is described as a function of density and Péclet

number), it gives an insufficient description of the spatial properties of the velocity field. To the best of our knowledge, a phase diagram obtained by changing the Péclet number through the persistence time as an alternative to the swim velocity has not been yet evaluated in the case of purely repulsive ABP. Our analysis suggests that a three-dimensional phase diagram is needed to characterize the phenomenology of active Brownian particles (at least, concerning the dynamical collective phenomena) and further investigations about the MIPS transition line or the solid–hexatic and hexatic–liquid transitions could be needed.

We have also explored the role of the inertial forces finding fascinating results that hold in solid configurations or the dense clusters of MIPS. Inertial forces introduce a typical time, τ_{I}, in addition to the persistence time of the active force. When the former is a larger one, the correlation length is decreased providing two main results: (i) inertia reduces the velocity alignment with respect to the overdamped case. (ii) The scaling of the correlation length with the persistence time is deeply affected. A linear regime, $\propto \tau$, for an initial broad interval of τ values, appears before the overdamped regime, scaling as $\propto \sqrt{\tau}$, and takes over as the persistence time becomes larger than the inertial time. Last but not least, we surprisingly observe a further non-equilibrium effect manifesting in the non-symmetric role of mass and inverse viscosity in the correlation length of the spatial velocity correlations. While the τ scaling is controlled by the inertial time, we show that the value of the correlation length explicitly depends on the mass and viscosity values separately and not only on their ratio (the inertial time). This observation suggests further investigations to test the role of the inertia on the phase diagram by varying both γ and m separately (and not just the inertial time), with particular attention to the coexistence line of the motility induced phase separation that could be deeply affected.

Finally, we highlight the non-thermal nature of the collective phenomenon described so far that is marginally affected by a temperature change, at variance with equilibrium models, such as the *XY* models. The increase of the solvent or active temperature leaves correlation length (and, thus, the size of the velocity domains) unchanged, at least in the dense configurations evaluated in this work. The use of T/T_{a} can be recognized as the dimensionless parameter necessary to compare the strengths of active force and thermal fluctuations. The increase of this ratio reduces the amplitude of the rescaled velocity correlation because of the T/T_{a} dependence on the kinetic temperature. We conclude that, to observe the velocity domains (or, equivalently, spatial structure in the velocity correlations), it is necessary to fix the solvent temperature rather smaller than the active temperature so that the active force term (that produces effective alignment interactions) is not overwhelmed by the uncorrelated thermal fluctuations.

Finally, we mention an interesting perspective concerning the generalization of our theory to active particles with attractive interactions.[84] Understanding how the dynamical scenario presented so far could be modified represents a challenging issue that could even shed light on the properties of the so-called living crystal scenario.[85–87] Even at small densities, attractive active particles are able to form clusters with hexatic or solid orders that move and rotate even in the steady-state. In this framework, the analysis of the velocity properties could provide further clues to understand the experimental phenomenology of active colloids.

Conflicts of interest

There are no conflicts to declare.

Appendix

A Overdamped ABP dynamics

In this Appendix, we report the numerical details employed to simulate overdamped ABP to measure the spatial velocity correlations shown in Fig. 2. Each particle is described by an equation of motion for its position $\boldsymbol{x}_i$:

$$\gamma \dot{\mathbf{x}}_i = \mathbf{F}_i + \mathbf{f}_i^{\mathrm{a}} + \sqrt{2\gamma m T}\eta_i, \tag{15}$$

where the parameters γ, T, m have the same physical meaning as in eqn (1).

The term η is a white noise vector with zero average and unit variance due to the collision by the solvent particles. The force term $\mathbf{F}_i$ models steric interactions between particles and is derived from the same potential used to simulate eqn (1). Finally, $\mathbf{f}_i^{\mathrm{a}}$ represents the active force that, in the literature based on ABP simulations, is usually expressed as

$$\mathbf{f}_i^{\mathrm{a}} = \gamma v_0 \mathbf{n}_i.$$

This is consistent with our notation and, in particular, with the swim velocity definition, eqn (5). In this system, the velocity vector employed to calculate the spatial velocity correlation function is obtained from the relation $\mathbf{v}_i = \dot{\mathbf{x}}_i$.

B Derivation of eqn (8)

In order to obtain the velocity correlation function in the Fourier space, *i.e.* eqn (8), we shall make two simplifying assumptions in eqn (1):

(i) We consider the AOUP model, assuming that $\mathbf{f}_i^{\mathrm{a}}$ evolves through eqn (7), an approximation often employed to obtain theoretical predictions of ABP numerical studies.

(ii) Each particle performs small oscillations around a node of a hexagonal lattice having a 6-fold symmetry.

(iii) Introducing the displacement $\mathbf{u}_i$ of particle i with respect to its lattice position, $\mathbf{x}_i^0$, namely

$$\mathbf{u}_i = \mathbf{x}_i - \mathbf{x}_i^0,$$

the interaction between a pair (i,j) of nearest neighbor particles is approximated by an elastic term of the form $U_{\mathrm{el}} = \frac{1}{2} m \omega_{\mathrm{E}}^2 (\mathbf{u}_i - \mathbf{u}_j)^2$ and the total inter-particle potential

reads:

$$U_{\mathrm{tot}} \approx m\frac{{\omega_{\mathrm{E}}}^2}{2}\sum_{i\neq j}\left(\mathbf{u}_i-\mathbf{u}_j\right)^2.$$

The frequency ω_{E} is given by:

$${\omega_{\mathrm{E}}}^2=\frac{1}{2m}\left(U''(\bar{x})+\frac{U'(\bar{x})}{\bar{x}}\right),$$

and its expression can be obtained following ref. 25. Here, the derivation is reported for completeness. Starting from the Taylor expansion of the non-linear potential, $U(r)$, the force can be approximated as:

$$\mathbf{F}(\mathbf{x}_i-\mathbf{x}_{i+j}) \approx -\hat{H}_j\cdot(\mathbf{u}_i-\boldsymbol{u}_{i+j}),$$

where the $\hat{H}_j$ are 2×2 matrices coupling the central particle to the j-th particle and are defined in terms of the second derivatives of the potential U:

$$\hat{H}_j=\begin{pmatrix} U_{xx}(\bar{\mathbf{r}}_{ij}) & U_{xy}(\bar{\mathbf{r}}_{ij}) \\ U_{yx}(\bar{\mathbf{r}}_{ij}) & U_{yy}(\bar{\mathbf{r}}_{ij})\end{pmatrix} \tag{16}$$

when the argument is $\bar{\mathbf{r}}_{ij}=\mathbf{x}_j^0-\mathbf{x}_i^0$. Explicitly, for the 6 nearest neighbour lattice nodes, we have $\bar{\mathbf{r}}_{ij}=\bar{r}\left(\cos\left(\frac{j\pi}{3}\right),\sin\left(\frac{j\pi}{3}\right)\right)$ for $j=1,6$. With these assumptions, we obtain:

$$\begin{aligned}
U_{xx}(\bar{\mathbf{r}}_{ij}) &= U''(\bar{r})\cos^2\left(j\frac{\pi}{3}\right)+\frac{U'(\bar{r})}{|\bar{r}|}\sin^2\left(j\frac{\pi}{3}\right)\\
U_{yy}(\bar{\mathbf{r}}_{ij}) &= U''(\bar{r})\sin^2\left(j\frac{\pi}{3}\right)+\frac{U'(\bar{r})}{|\bar{r}|}\cos^2\left(j\frac{\pi}{3}\right)\\
U_{xy}(\bar{\mathbf{r}}_{ij}) &= U_{yx}(\bar{\mathbf{r}}_{ij})=\left[U''(\bar{r})-\frac{U'(\bar{r})}{|\bar{r}|}\right]\cos\left(j\frac{\pi}{3}\right)\sin\left(j\frac{\pi}{3}\right).
\end{aligned}$$

As shown in the ESI of ref. 25, in the solid configurations, the matrix $\hat{H}_j$ can be approximated by its average over the 6 neighboring particles, $\bar{h}$, so that the force acting on the particle i reads:

$$\mathbf{F}_i \approx -\sum_j \hat{H}_j\cdot\left(\mathbf{u}_i-\mathbf{u}_{i+j}\right)\approx -\bar{h}\sum_j\left(\mathbf{u}_i-\mathbf{u}_{i+j}\right),$$

where

$$\bar{h}=\frac{1}{6}\sum_j\hat{H}_j=\frac{1}{2}\left[U''(\bar{r})+\frac{U'(\bar{r})}{|\bar{r}|}\right]\hat{I}=m{\omega_{\mathrm{E}}}^2\hat{I}$$

In which $\hat{I}$ is the identity matrix. Therefore, the equations of motion become:

$$\dot{\mathbf{v}}_i=-\frac{\gamma}{m}\mathbf{v}_i-{\omega_{\mathrm{E}}}^2\sum_j^{\mathrm{n.n}}\left(\mathbf{u}_i-\mathbf{u}_j\right)+\frac{\mathbf{f}_i^{\mathrm{a}}}{m}+\sqrt{2\frac{\gamma}{m}T}\eta_i \tag{17a}$$

$$\dot{\mathbf{f}}_i^{\mathrm{a}}=-\frac{1}{\tau}\mathbf{f}_i^{\mathrm{a}}+\sqrt{\frac{2}{\tau}}f_0\mathbf{x}_i, \tag{17b}$$

where the sum is over nearest neighbour only. To proceed further, we introduce the discrete Fourier transforms of the displacement about the lattice positions, velocity and active force, $\hat{\mathbf{u}}(\boldsymbol{q})$, $\hat{\mathbf{v}}(\boldsymbol{q})$, and $\hat{\mathbf{f}}^{\mathrm{a}}(\boldsymbol{q})$, respectively. They are defined as:

$$\begin{aligned}
\hat{\mathbf{u}}(\mathbf{q}) &= \frac{1}{N}\sum_j\mathbf{u}_j\mathrm{e}^{-i\mathbf{q}\cdot\mathbf{x}_i^0}\\
\hat{\mathbf{v}}(\mathbf{q}) &= \frac{1}{N}\sum_j\mathbf{v}_j\mathrm{e}^{-i\mathbf{q}\cdot\mathbf{x}_i^0}\\
\hat{\mathbf{f}}^{\mathrm{a}}(\mathbf{q}) &= \frac{1}{N}\sum_j\mathbf{f}_j^{\mathrm{a}}\mathrm{e}^{-i\mathbf{q}\cdot\mathbf{x}_i^0}
\end{aligned}$$

where i is the imaginary unit and $\mathbf{q}=(q_x,q_y)$ are the Cartesian components of the vectors of the reciprocal Bravais lattice. The equations of motion (17) in the Fourier space become:

$$\frac{\mathrm{d}}{\mathrm{d}t}\hat{\mathbf{v}}(\mathbf{q})=-\frac{\gamma}{m}\hat{\mathbf{v}}(\mathbf{q})-\omega^2(\mathbf{q})\hat{\mathbf{u}}(\mathbf{q})+\frac{\hat{\mathbf{f}}^{\mathrm{a}}(\mathbf{q})}{m}+\sqrt{2\gamma\frac{T}{m}}\hat{\eta}(\mathbf{q}) \tag{18a}$$

$$\tau\frac{\mathrm{d}}{\mathrm{d}t}\hat{\mathbf{f}}^{\mathrm{a}}(\mathbf{q})=-\hat{\mathbf{f}}^{\mathrm{a}}(\mathbf{q})+f_0\sqrt{2\tau}\hat{\xi}(\mathbf{q}), \tag{18b}$$

where the frequency $\omega^2(\mathbf{q})$ reads:

$$\begin{aligned}
\omega^2(\mathbf{q}) &= -2{\omega_{\mathrm{E}}}^2\left[\cos(q_x\bar{x})+2\cos\left(\frac{1}{2}q_x\bar{x}\right)\cos\left(\frac{\sqrt{3}}{2}q_y\bar{x}\right)-3\right]\\
&\approx\frac{3}{2}{\omega_{\mathrm{E}}}^2\bar{x}^2\mathbf{q}^2+O(\mathbf{q}^4),
\end{aligned} \tag{19}$$

and in the last line, we have performed a Taylor expansion around $\mathbf{q}=0$. Solving the dynamics (18), we get the final expression for the positional correlation function:

$$\langle\hat{\mathbf{u}}(\mathbf{q})\cdot\hat{\mathbf{u}}(-\mathbf{q})\rangle=\frac{2T}{m\omega^2(\mathbf{q})}+\frac{2{f_0}^2}{m\omega^2(\mathbf{q})}\frac{\tau}{\gamma}\frac{1}{1+\dfrac{\tau^2}{1+\tau/\tau_{\mathrm{I}}}\omega^2(\mathbf{q})}$$

and the velocity correlation functions:

$$\langle\hat{\mathbf{v}}(\mathbf{q})\cdot\hat{\mathbf{v}}(-\mathbf{q})\rangle=\frac{2T}{m}+\frac{2{f_0}^2}{m}\frac{\tau}{\gamma}\frac{1}{1+\tau/\tau_{\mathrm{I}}}\frac{1}{1+\dfrac{\tau^2}{1+\tau/\tau_{\mathrm{I}}}\omega^2(\mathbf{q})}, \tag{20}$$

both evaluated in the Fourier space. Eqn (20) coincides with eqn (8) using the definition of T_{a}.

C Derivation of eqn (10)

The velocity real space correlation, *i.e.* eqn (10), is obtained by inverting formula (20):

$$\langle\mathbf{v}_{\mathbf{x}}\cdot\mathbf{v}_{\mathbf{x}'}\rangle=\frac{2T}{m}\delta_{\mathbf{x},\mathbf{x}'}+\frac{2{f_0}^2}{m}\frac{\tau}{\gamma}\frac{1}{1+\tau/\tau_{\mathrm{I}}}\sum_{\mathbf{q}}\frac{\mathrm{e}^{i\mathbf{q}(\mathbf{x}-\mathbf{x}')}}{1+\dfrac{\tau^2}{1+\tau/\tau_{\mathrm{I}}}\omega^2(\mathbf{q})} \tag{21}$$

For large particle separations, $r=|\mathbf{x}-\mathbf{x}'|>\sigma$, the first term is negligible while the second term can be evaluated by performing the following approximations: (i) the finite lattice sum is replaced by a double integral over (q_x,q_y) variables, (ii) the frequency is replaced by its small $\mathbf{q}$-expansion and (iii) the limits of integration are extended from $-\infty$ to ∞. Using these

approximations, we have:

$$\langle \mathbf{v}_\mathbf{x} \cdot \mathbf{v}_{\mathbf{x}'} \rangle \approx 2\frac{{f_0}^2\tau}{m\gamma}\frac{1}{2\pi}\frac{\bar{x}^2}{\lambda^2}\frac{1}{1+\frac{\tau}{\tau_\mathrm{I}}}K_0(r/\lambda),$$

where the coherence length (or correlation length) λ is given by:

$$\lambda^2 \equiv \frac{3}{2}\bar{x}^2\frac{{\omega_\mathrm{E}}^2\tau^2}{1+\frac{\tau}{\tau_\mathrm{I}}} \tag{22}$$

and $K_0(r/\lambda)$ is the zero-order modified Bessel function of the second kind which has the following asymptotic behavior when $r/\lambda \gg 1$:

$$K_0(r/\lambda) \approx \left(\frac{\pi\lambda}{2r}\right)^{1/2} \mathrm{e}^{-r/\lambda}.$$

Therefore, for large separations, we find the following approximation:

$$\langle \mathbf{v}_\mathbf{x} \cdot \mathbf{v}_{\mathbf{x}'} \rangle \approx 2\frac{{f_0}^2\tau}{m\gamma}\frac{1}{1+\frac{\tau}{\tau_\mathrm{I}}}\frac{\bar{x}^2}{\lambda^2}\left(\frac{\lambda}{8\pi r}\right)^{1/2}\mathrm{e}^{-r/\lambda}. \tag{23}$$

Switching to a continuous notation such that $\mathbf{v}_\mathbf{x} \to \mathbf{v}(\mathbf{x})$, fixing $r = |\mathbf{x} - \mathbf{x}'|$ and formally dividing by the velocity variance $\langle {\mathbf{v}_\mathbf{x}}^2 \rangle$, we obtain eqn (10) after using the definition of T_a while eqn (22) coincides with eqn (11).

D Kinetic temperature: eqn (12)

To obtain an analytical expression for the kinetic temperature, we need to calculate eqn (21) in $r = |\mathbf{x} - \mathbf{x}'| = 0$. In this case, we need to consider the exact expression of $\omega^2(\mathbf{q})$ without employing any small $\mathbf{q}$ expansion. We replace the sum by a double integral over a finite domain:

$$\langle \mathbf{v}_\mathbf{x} \cdot \mathbf{v}_\mathbf{x} \rangle = \frac{2T}{m} + \frac{2{f_0}^2}{m}\frac{\tau}{\gamma}\frac{1}{1+\tau/\tau_\mathrm{I}+6{\omega_\mathrm{E}}^2\tau^2}\int_{-\pi}^{\pi}\frac{\mathrm{d}k_1}{2\pi}\int_{-\pi}^{\pi}\frac{\mathrm{d}k_2}{2\pi}\frac{1}{1-zs(k_1,k_2)}$$

where we have performed a change of variables of integration and introduced $s(k_1,k_2)$, the so-called structure function of the triangular lattice:[88]

$$s(k_1,k_2) = \frac{1}{3}(\cos(k_1)+\cos(k_2)+\cos(k_1+k_2)),$$

with

$$z = \frac{1}{1+\frac{1+\tau/\tau_\mathrm{I}}{6{\omega_\mathrm{E}}^2\tau^2}}.$$

In detail, one can evaluate the integral as:

$$\int_{-\pi}^{\pi}\frac{\mathrm{d}k_1}{2\pi}\int_{-\pi}^{\pi}\frac{\mathrm{d}k_2}{2\pi}\frac{1}{1-zs(k_1,k_2)} = \frac{6}{\pi z\sqrt{c}}\mathbf{K}(k),$$

where $\mathbf{K}(k)$ is the complete elliptic integral of the first kind:

$$\mathbf{K}(k) = \int_0^{\pi/2}\frac{\mathrm{d}\theta}{\sqrt{1-k^2\sin^2(\theta)}},$$

with

$$c = \frac{9}{z^2} - 3 + \sqrt{3+\frac{6}{z}}$$

$$k = 2\frac{\left(3+\frac{6}{z}\right)^{1/4}}{c^{1/2}}.$$

Hence, in the limit $\tau \to \infty$, we have $z \to 1$ and the integral in eqn (24) weakly (in fact, logarithmically) diverges for any two-dimensional lattice, being connected to the fact that the probability of returning to the origin by a random walker in two dimensions is certain. However, in the same limit, the dependence on τ of the prefactor in front of the integral makes the resulting contribution of the self-propulsion to the velocity variance vanishingly small. This can be seen as a consequence of the well-known fact that the velocity of active particles also depends on the forces they experience in such a way that they are slower in those regions where the curvature of the local potential is high. Finally, upon defining:

$$\mathscr{J} = \frac{6}{z\sqrt{c}}\mathbf{K}(k),$$

we get the exact expression for the kinetic temperature reported in eqn (10). Because of the definitions of k, c and z, the term depends only on τ, τ_I and ω_E and, thus, is independent of T and T_a.

E Solid–hexatic transition and decrease of λ

In this Appendix, we confirm the study of ref. 26 also in the underdamped ABP showing that, when the solid–hexatic transition takes place, an abrupt decrease of λ occurs with respect to prediction (12). However, here, the solid–hexatic transition is approached by increasing v_0 (at constant D_r) as in ref. 69, while in ref. 26 this has been obtained by decreasing $D_\mathrm{r} = 1/\tau$.

Following ref. 26 and 69, we monitor the structural properties of the system investigating the behavior of the orientational order parameter, $\Psi_6(\mathbf{x}_i)$. This is defined as $\Psi_6(\mathbf{x}_i) = \sum_j \mathrm{e}^{6i\alpha_{ij}}/N_i$, where the sum is restricted to the first neighbors of particle i, namely, N_i and α_{ij} is the angle – with respect to the x axis – of the segment joining the i-th and the j-th particle. To distinguish between solid and hexatic phases, we focus on the correlation function of $\Psi_6(\mathbf{x}_i)$:

$$g_6\big(r = |\mathbf{x}_i - \mathbf{x}_j|\big) = \big\langle \Psi_6(\mathbf{x}_i)\Psi_6^*(\mathbf{x}_j)\big\rangle / \big\langle {\Psi_6}^2(\mathbf{x}_j)\big\rangle. \tag{24}$$

Indeed, $g_6(r)$ is roughly constant in the solid phase, while decays roughly as a power law in the hexatic phase. Fig. 5 shows the value of $g_6(r)$ for the configurations reported in Fig. 5. This analysis confirms that for $v_0 \leq 50$ (corresponding to $f_0 = 5 \times 10^3$ and Pe = 5, $D_\mathrm{r} = 10$) the system is in the solid configuration since

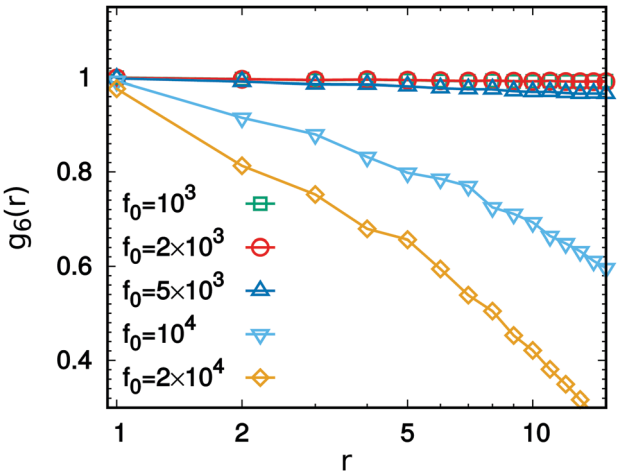

Fig. 5 Panel (a): Spatial correlation of the orientational order parameter, $g_6(r)$, defined by eqn (24), for different values of the self-propulsion intensity, $f_0 = v_0\gamma$. The simulations are obtained with the same parameters of Fig. 2 to show that the correlation length, λ, starts decreasing when the solid–hexatic transition takes place; in particular, $\phi = 1.1$, $N = 10^4$, $\gamma = 10^2$, $m = 1$, $\varepsilon = 10^2$, $\sigma = 1$, $T = 10^{-1}$ and $D_r = 10$. In this way, v_0 ranges from 10 to 200 corresponding to a range of Péclet numbers from 1 to 20. In particular, the solid–hexatic transition is observed for $10 > \mathrm{Pe} > 5$ (corresponding to $10^4 > f_0 > 5 \times 10^3$ and $10^2 > v_0 \geq 50$).

the function $g_6(r)$ is almost independent of r, while starting from $v_0 = 10^2$ (corresponding to $f_0 = 10^4$ and Pe = 10, $D_r = 10$), the system attains hexatic configurations because $g_6(r)$ decays algebraically. We also comment that the solid–hexatic transition point, here occurring for $5 < \mathrm{Pe}^* < 10$, could depend on the specific value of D_r considered in the numerical study since there is no numerical or theoretical evidence that mapping the increase of v_0 onto the decrease of D_r leaves the solid–hexatic transition unchanged.

Acknowledgements

LC and UMBM acknowledge support from the MIUR PRIN 2017 project 201798CZLJ. LC and UMBM warmly thank Andrea Puglisi for letting them use the computer facilities of his group and for discussions regarding some aspects of this research.

Notes and references

1 M. Marchetti, J. Joanny, S. Ramaswamy, T. Liverpool, J. Prost, M. Rao and R. A. Simha, *Rev. Mod. Phys.*, 2013, **85**, 1143–1189.
2 J. Elgeti, R. G. Winkler and G. Gompper, *Rep. Prog. Phys.*, 2015, **78**, 056601.
3 G. Gompper, R. G. Winkler, T. Speck, A. Solon, C. Nardini, F. Peruani, H. Löwen, R. Golestanian, U. B. Kaupp and L. Alvarez, *et al.*, *J. Phys.: Condens. Matter*, 2020, **32**, 193001.
4 T. Van Noije, M. Ernst, E. Trizac and I. Pagonabarraga, *Phys. Rev. E: Stat. Phys., Plasmas, Fluids, Relat. Interdiscip. Top.*, 1999, **59**, 4326.
5 A. Baldassarri, U. M. B. Marconi and A. Puglisi, *Phys. Rev. E: Stat., Nonlinear, Soft Matter Phys.*, 2002, **65**, 051301.
6 C. Dombrowski, L. Cisneros, S. Chatkaew, R. E. Goldstein and J. O. Kessler, *Phys. Rev. Lett.*, 2004, **93**, 098103.
7 F. Peruani, J. Starruß, V. Jakovljevic, L. Søgaard-Andersen, A. Deutsch and M. Bär, *Phys. Rev. Lett.*, 2012, **108**, 098102.
8 H. Wioland, F. G. Woodhouse, J. Dunkel and R. E. Goldstein, *Nat. Phys.*, 2016, **12**, 341–345.
9 H. H. Wensink, J. Dunkel, S. Heidenreich, K. Drescher, R. E. Goldstein, H. Löwen and J. M. Yeomans, *Proc. Natl. Acad. Sci. U. S. A.*, 2012, **109**, 14308–14313.
10 J. Dunkel, S. Heidenreich, K. Drescher, H. H. Wensink, M. Bär and R. E. Goldstein, *Phys. Rev. Lett.*, 2013, **110**, 228102.
11 J. Urzay, A. Doostmohammadi and J. Yeomans, *J. Fluid Mech.*, 2017, **822**, 762–773.
12 M. James, W. J. Bos and M. Wilczek, *Phys. Rev. Fluids*, 2018, **3**, 061101.
13 R. Großmann, P. Romanczuk, M. Bär and L. Schimansky-Geier, *Phys. Rev. Lett.*, 2014, **113**, 258104.
14 R. Großmann, I. S. Aranson and F. Peruani, *Nat. Commun.*, 2020, **11**, 1–12.
15 L. Petitjean, M. Reffay, E. Grasland-Mongrain, M. Poujade, B. Ladoux, A. Buguin and P. Silberzan, *Biophys. J.*, 2010, **98**, 1790–1800.
16 M. A. Heinrich, R. Alert, J. M. LaChance, T. J. Zajdel, A. Košmrlj and D. J. Cohen, *eLife*, 2020, **9**, e58945.
17 C. Blanch-Mercader, V. Yashunsky, S. Garcia, G. Duclos, L. Giomi and P. Silberzan, *Phys. Rev. Lett.*, 2018, **120**, 208101.
18 S. Henkes, K. Kostanjevec, J. M. Collinson, R. Sknepnek and E. Bertin, *Nat. Commun.*, 2020, **11**, 1–9.
19 S. Garcia, E. Hannezo, J. Elgeti, J.-F. Joanny, P. Silberzan and N. S. Gov, *Proc. Natl. Acad. Sci. U. S. A.*, 2015, **112**, 15314–15319.
20 M. Basan, J. Elgeti, E. Hannezo, W.-J. Rappel and H. Levine, *Proc. Natl. Acad. Sci. U. S. A.*, 2013, **110**, 2452–2459.
21 R. Alert and X. Trepat, *Annu. Rev. Condens. Matter Phys.*, 2020, **11**, 77–101.
22 N. Sepúlveda, L. Petitjean, O. Cochet, E. Grasland-Mongrain, P. Silberzan and V. Hakim, *PLoS Comput. Biol.*, 2013, **9**, e1002944.
23 D. Sarkar, G. Gompper and J. Elgeti, 2020, arXiv preprint arXiv:2006.04519.
24 B. Smeets, R. Alert, J. Pešek, I. Pagonabarraga, H. Ramon and R. Vincent, *Proc. Natl. Acad. Sci. U. S. A.*, 2016, **113**, 14621–14626.
25 L. Caprini, U. M. B. Marconi and A. Puglisi, *Phys. Rev. Lett.*, 2020, **124**, 078001.
26 L. Caprini, U. M. B. Marconi, C. Maggi, M. Paoluzzi and A. Puglisi, *Phys. Rev. Res.*, 2020, **2**, 023321.
27 L. Caprini and U. M. B. Marconi, *Phys. Rev. Res.*, 2020, **2**, 033518.
28 M. E. Cates and J. Tailleur, *Annu. Rev. Condens. Matter Phys.*, 2015, **6**, 219–244.
29 G. Gonnella, D. Marenduzzo, A. Suma and A. Tiribocchi, *C. R. Phys.*, 2015, **16**, 316–331.

30 J. Bialké, T. Speck and H. Löwen, *J. Non-Cryst. Solids*, 2015, **407**, 367–375.
31 C. B. Caporusso, P. Digregorio, D. Levis, L. F. Cugliandolo and G. Gonnella, *Phys. Rev. Lett.*, 2020, **125**, 178004.
32 U. M. B. Marconi, N. Gnan, M. Paoluzzi, C. Maggi and R. Di Leonardo, *Sci. Rep.*, 2016, **6**, 23297.
33 L. Caprini and U. M. B. Marconi, *Soft Matter*, 2018, **14**, 9044–9054.
34 S. Das, G. Gompper and R. G. Winkler, *New J. Phys.*, 2018, **20**, 015001.
35 L. Caprini and U. M. B. Marconi, *Soft Matter*, 2019, **15**, 2627–2637.
36 É. Fodor, C. Nardini, M. E. Cates, J. Tailleur, P. Visco and F. van Wijland, *Phys. Rev. Lett.*, 2016, **117**, 038103.
37 U. M. B. Marconi, A. Puglisi and C. Maggi, *Sci. Rep.*, 2017, **7**, 46496.
38 L. Caprini, U. M. B. Marconi, A. Puglisi and A. Vulpiani, *J. Stat. Mech.: Theory Exp.*, 2019, **2019**, 053203.
39 L. Dabelow and R. Eichhorn, *Frontiers in Physics*, 2021, **8**, 516.
40 C. Maggi, M. Paoluzzi, A. Crisanti, E. Zaccarelli and N. Gnan, *Soft Matter*, 2021, Advance Article.
41 C. Bechinger, R. Di Leonardo, H. Löwen, C. Reichhardt, G. Volpe and G. Volpe, *Rev. Mod. Phys.*, 2016, **88**, 045006.
42 H. Löwen, *J. Chem. Phys.*, 2020, **152**, 040901.
43 S. Mandal, B. Liebchen and H. Löwen, *Phys. Rev. Lett.*, 2019, **123**, 228001.
44 L. Caprini and U. Marini Bettolo Marconi, *J. Chem. Phys.*, 2021, **154**, 024902.
45 I. Petrelli, L. F. Cugliandolo, G. Gonnella and A. Suma, *Phys. Rev. E*, 2020, **102**, 012609.
46 C. Dai, I. R. Bruss and S. C. Glotzer, *Soft Matter*, 2020, **16**, 2847–2853.
47 J. Su, H. Jiang and Z. Hou, 2020, arXiv preprint arXiv:2009.03697x.
48 H. D. Vuijk, J.-U. Sommer, H. Merlitz, J. M. Brader and A. Sharma, *Phys. Rev. Res.*, 2020, **2**, 013320.
49 C. Scholz, S. Jahanshahi, A. Ldov and H. Löwen, *Nat. Commun.*, 2018, **9**, 1–9.
50 O. Dauchot and V. Démery, *Phys. Rev. Lett.*, 2019, **122**, 068002.
51 M. Leoni, M. Paoluzzi, S. Eldeen, A. Estrada, L. Nguyen, M. Alexandrescu, K. Sherb and W. W. Ahmed, *Phys. Rev. Res.*, 2020, **2**, 043299.
52 G. S. Redner, M. F. Hagan and A. Baskaran, *Phys. Rev. Lett.*, 2013, **110**, 055701.
53 M. R. Shaebani, A. Wysocki, R. G. Winkler, G. Gompper and H. Rieger, *Nat. Rev. Phys.*, 2020, 1–19.
54 L. Dabelow, S. Bo and R. Eichhorn, *Phys. Rev. X*, 2019, **9**, 021009.
55 L. Berthier, E. Flenner and G. Szamel, *J. Chem. Phys.*, 2019, **150**, 200901.
56 L. Berthier, E. Flenner and G. Szamel, *New J. Phys.*, 2017, **19**, 125006.
57 C. Maggi, M. Paoluzzi, N. Pellicciotta, A. Lepore, L. Angelani and R. Di Leonardo, *Phys. Rev. Lett.*, 2014, **113**, 238303.
58 E. Woillez, Y. Kafri and V. Lecomte, *J. Stat. Mech.: Theory Exp.*, 2020, **2020**, 063204.
59 L. Caprini, U. Marini Bettolo Marconi, A. Puglisi and A. Vulpiani, *J. Chem. Phys.*, 2019, **150**, 024902.
60 R. Wittmann and J. M. Brader, *EPL*, 2016, **114**, 68004.
61 D. Martin, J. O'Byrne, M. E. Cates, É. Fodor, C. Nardini, J. Tailleur and F. van Wijland, 2020, arXiv preprint arXiv:2008.12972.
62 C. Maggi, M. Paoluzzi, L. Angelani and R. Di Leonardo, *Sci. Rep.*, 2017, **7**, 1–7.
63 L. Caprini, U. M. B. Marconi and A. Vulpiani, *J. Stat. Mech.: Theory Exp.*, 2018, **2018**, 033203.
64 G. Szamel, *Phys. Rev. E: Stat., Nonlinear, Soft Matter Phys.*, 2014, **90**, 012111.
65 T. F. Farage, P. Krinninger and J. M. Brader, *Phys. Rev. E: Stat., Nonlinear, Soft Matter Phys.*, 2015, **91**, 042310.
66 L. Caprini, E. Hernández-Garca, C. López and U. M. B. Marconi, *Sci. Rep.*, 2019, **9**, 1–13.
67 L. Caprini and U. Marini Bettolo Marconi, *J. Chem. Phys.*, 2020, **153**, 184901.
68 J. Bialké, T. Speck and H. Löwen, *Phys. Rev. Lett.*, 2012, **108**, 168301.
69 P. Digregorio, D. Levis, A. Suma, L. F. Cugliandolo, G. Gonnella and I. Pagonabarraga, *Phys. Rev. Lett.*, 2018, **121**, 098003.
70 Y. Fily and M. C. Marchetti, *Phys. Rev. Lett.*, 2012, **108**, 235702.
71 M. E. Cates and J. Tailleur, *EPL*, 2013, **101**, 20010.
72 I. Buttinoni, J. Bialké, F. Kümmel, H. Löwen, C. Bechinger and T. Speck, *Phys. Rev. Lett.*, 2013, **110**, 238301.
73 J. Stenhammar, R. Wittkowski, D. Marenduzzo and M. E. Cates, *Phys. Rev. Lett.*, 2015, **114**, 018301.
74 A. P. Solon, J. Stenhammar, R. Wittkowski, M. Kardar, Y. Kafri, M. E. Cates and J. Tailleur, *Phys. Rev. Lett.*, 2015, **114**, 198301.
75 S. A. Mallory, C. Valeriani and A. Cacciuto, *Annu. Rev. Phys. Chem.*, 2018, **69**, 59–79.
76 X.-q. Shi, G. Fausti, H. Chaté, C. Nardini and A. Solon, *Phys. Rev. Lett.*, 2020, **125**, 168001.
77 A. M. Menzel and H. Löwen, *Phys. Rev. Lett.*, 2013, **110**, 055702.
78 A. M. Menzel, T. Ohta and H. Löwen, *Phys. Rev. E: Stat., Nonlinear, Soft Matter Phys.*, 2014, **89**, 022301.
79 G. Briand, M. Schindler and O. Dauchot, *Phys. Rev. Lett.*, 2018, **120**, 208001.
80 J. Stenhammar, D. Marenduzzo, R. J. Allen and M. E. Cates, *Soft Matter*, 2014, **10**, 1489–1499.
81 A. Costanzo, J. Elgeti, T. Auth, G. Gompper and M. Ripoll, *EPL*, 2014, **107**, 36003.
82 D. R. Rodriguez, F. Alarcon, R. Martinez, J. Ramrez and C. Valeriani, *Soft Matter*, 2020, **16**, 1162–1169.
83 J. Martin, R. Martinez, L. C. Alexander, A. L. Diez, D. G. Aarts, F. Alarcon, J. Ramirez and C. Valeriani, 2020, arXiv preprint arXiv:2012.07087.
84 G. Redner, A. Baskaran and M. Hagan, *Phys. Rev. E: Stat., Nonlinear, Soft Matter Phys.*, 2013, **88**, 012305.

85 J. Palacci, S. Sacanna, A. P. Steinberg, D. J. Pine and P. M. Chaikin, *Science*, 2013, **339**, 936–940.
86 B. M. Mognetti, A. Šarić, S. Angioletti-Uberti, A. Cacciuto, C. Valeriani and D. Frenkel, *Phys. Rev. Lett.*, 2013, **111**, 245702.
87 M. N. Van Der Linden, L. C. Alexander, D. G. Aarts and O. Dauchot, *Phys. Rev. Lett.*, 2019, **123**, 098001.
88 A. J. Guttmann, *J. Phys. A: Math. Theor.*, 2010, **43**, 305205.